Computational Analysis and Optimization of a Chemical Vapor Deposition Reactor with Large-Scale Computing

Andrew G. Salinger*, Roger P. Pawlowski, John N. Shadid,
and Bart van Bloemen Waanders
Sandia National Laboratories†

February 9, 2004

Abstract

A computational analysis and optimization is presented for the chemical vapor deposition (CVD) of silicon in a horizontal rotating disk reactor. A three-dimensional reactor-scale model for the gas flow, heat transfer, and mass transfer in a CVD reactor is coupled to a simple transport-limited surface reaction mechanism for the deposition of epitaxial silicon from trichlorosilane. The model is solved to steady-state for the deposition rate profile over the 8-inch silicon wafer using an unstructured grid finite element method and a fully coupled inexact Newton method on parallel computers. Since a high degree of spatial uniformity in the deposition rate is desired, parameter continuation runs for 6 key operating parameters, including the inlet flow rate and the rotation rate of the substrate, were performed and their individual effects analyzed. Finally, optimization runs were performed that located operating conditions that predict non-uniformity as low as 0.1%.

*Corresponding author (who in 1994 had the privilege of being a NATO Postdoctoral Fellow under Prof. Eigenberger at ICVT, University of Stuttgart): Sandia National Laboratories, P.O. Box 5800, MS-1111, Albuquerque, NM, 87185 USA. Tel:(505)845-3523. email:agsalin@sandia.gov.

†This work was funded by Sandia's LDRD program and the Mathematical, Information, and Computational Sciences Program of the U.S. DOE Office of Science. Sandia is a multiprogram laboratory operated by Sandia Corporation, a Lockheed-Martin Company, for the United States Department of Energy under Contract DE-AC04-94AL85000

1 Introduction

In this paper we present an analysis and optimization of a three-dimensional model of a horizontal chemical vapor deposition (CVD) reactor used in the deposition of epitaxial silicon from trichlorosilane (TCS). This work demonstrates that robust numerical methods for the efficient solution of nonlinear partial differential equations (PDEs) on parallel computers can be integrated with continuation and optimization algorithms to enable a rapid and thorough analysis of a complex, three-dimensional chemical reactor model. The focus of the analysis is to determine the influence of several key operating parameters on the spatial uniformity of the deposition rate of epitaxial silicon.

As the size of modern microelectronic components continue to be reduced, more stable and improved reactor designs are needed to maintain required tolerances in deposition uniformity. The experimental modifications of reactor configurations and manual control of operating conditions becomes prohibitively expensive and time consuming. Furthermore, small sample spaces in experimental data can mask trends in operating parameters. Computer simulation can help to elucidate these trends and allow designers to evaluate numerous reactor configurations.

It has been demonstrated that, for horizontal reactors, three-dimensional models are typically required to capture critical physical phenomena.[1–4] Therefore, high-performance computing with efficient numerical methods are required. There are now several demonstrations of such large-scale simulation design studies in the literature.[4–8] Kommu *et al.*[7] finish their paper with a demonstration how deposition rate uniformity can be strongly effected by the inlet flow profile, but is not effected by wafer rotation rates under 50rpm. In this work we continue their analysis of the effects of operating parameters on deposition rate uniformity by performing detailed parameter studies.

For a number of years, our research group has been among those working on developing numerical algorithms and computer codes for efficient, robust, and scalable solution of coupled nonlinear PDEs on parallel computers. This work centers on the chemically reacting flow code MPSalsa, which implements an unstructured grid finite element method on distributed-memory parallel computers (details and references in Section 3). MPSalsa uses a fully-coupled Newton algorithm for the nonlinear solution, which relies on parallel preconditioned iterative linear solvers (contained in the Aztec code[9]) to solve the resulting linear system. The investment in calculating, storing, and solving the Jacobian matrix for Newton's method leads to a robust steady-state solution capability. The robustness and accuracy of a Newton solution algorithm enables the use of sophisticated analysis algorithms such as parameter continuation (performed here with the LOCA code[10]) and

optimization algorithms (using the Dakota framework[11]). Our previous work in CVD optimization includes preliminary results for $GaAs$ deposition in a low-pressure 3D reactor[12] and for a 2D model of GaN deposition.[13,14]

This work is unique in performing optimization of a 3D Silicon reactor over several parameters. The model includes some of the geometric complexity of industrial reactors, and notably includes the effect of the purge gas entering between the rotating substrate and the fixed reactor. We have employed a simple transport limited mechanism for silicon deposition. This choice helped assure that we could explore the parameter space thoroughly and have the necessary robustness to perform optimization calculations. Future studies will consider more complex and rigorous chemistry mechanisms, several of which are available.[7,15–19]

While the limitations in the model prevent it from being predictive for any specific reactor, the optimization calculations do show how non-uniformity in deposition rate can be driven very low by balancing the effects of the different parameters. It is evident that this could not be done efficiently by searching parameter space manually. The parameter continuation studies do reveal trends that could aid others in interpreting both experimental and numerical results for similar reactors.

In Section 2 we present our model for the growth of silicon in a horizontal CVD reactor. This includes a description of the reactor geometry, the PDE model, and the operating parameters that will be varied in the results sections. The numerical solution algorithms are presented in Section 3. In Section 4 we present the solutions to the model at some base operating conditions and then the result of 6 parameters studies, which detail the effect of these parameters on the uniformity of silicon growth rates over the wafer surface. Finally in Section 5, we present results from performing optimization runs on those 6 parameters to achieve uniform silicon film growth over the wafer.

2 Reactor Model

The simulations in this paper are for the deposition of silicon from TCS in a horizontal CVD reactor with a rotating susceptor. The description of the reactor geometry and operation is described in Section 2.1. The partial differential equations and reaction mechanism that approximate the real physics in the reactor are presented in Section 2.2. The boundary conditions, which include the 6 parameters varied in the analysis, are presented in Section 2.3.

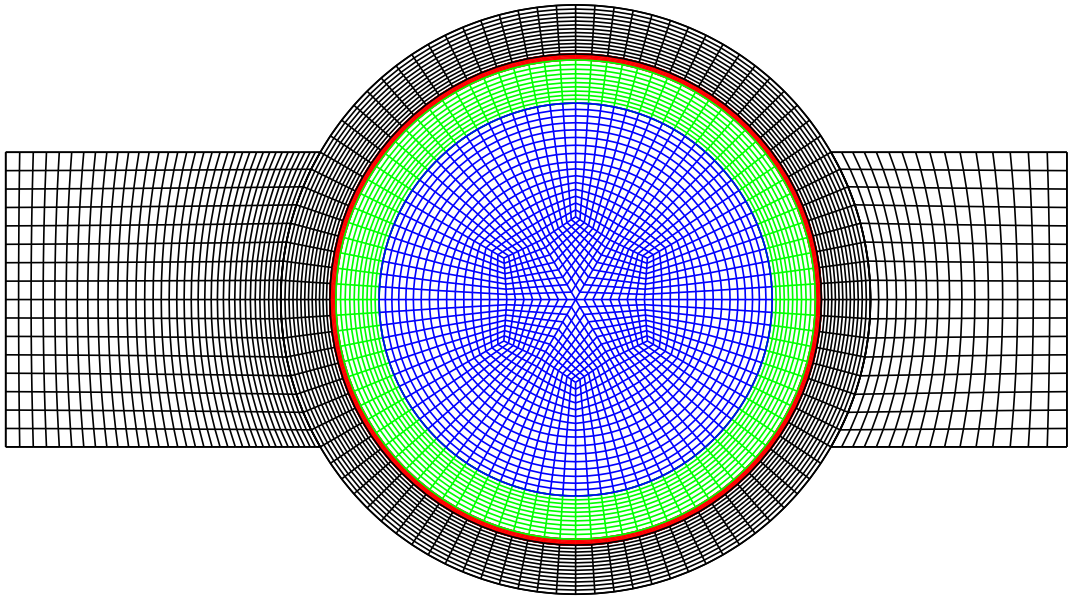

Figure 1: The surface mesh for the bottom of the reactor is shown. The flow enters at the left end and exits at the right. A thin, annular gap region separates the rotating wafer and susceptor surfaces from the fixed part of the reactor, which consist of the outer annular region and two rectangular sections. The height of the reactor (not shown) is a constant.

2.1 Problem Description

This paper models the chemical vapor deposition (CVD) of silicon on a 200mm (8 inch) wafer from trichlorosilane (TCS) in a hydrogen, H_2, carrier gas. We model the three-dimensional reactor chamber, which consists of a cylindrical main chamber, a rectangular inlet section, and a rectangular outlet section. A view of the bottom of the reactor (with the finite element discretization) is shown in Figure 1. Our model does not include variations in the height of the reactor in the inlet and outlet sections, though these can exist in industrial reactors.[7]

A mixture of TCS and H_2 enters the reactor at the left end and exit through the right end. The susceptor and wafer surfaces (which are treated identically in the model until post-processing) are held at a fixed elevated temperature which promotes surface reactions producing the deposition of a solid silicon thin film. These surfaces also rotate to counter the effects of reactant depletion along the flow direction that leads to a decreasing deposition rate through the length of the reactor.

Rotation also effects the flow profiles. Between the rotating susceptor and the fixed part of the reactor is an annular gap, where a purge flow of pure H_2 can be injected to prevent silicon depositing underneath the disk and interfering with the rotation mechanism. The rest of the reactor is not actively heated or cooled, but the temperature of the top of the reactor is set in the model for reasons detailed below.

The reactor is configured as follows. The wafer is centered at the bottom of the reactor and has a radius of $r < 10cm$. Moving radially outward, there is the susceptor region and then a narrow annular gap which forms the break between the rotating and fixed section of the reactor. The rest of the cylindrical chamber extends out to $r < 15cm$. The entrance and exit rectangular sections have widths of $15cm$ with the entrance (on the left in Figure 1) having length of $16cm$ and the exit of length $12cm$. The height of the reactor (not shown in this figure) is a uniform $3cm$, so the pictured geometry and mesh are simply extruded in the third dimension.

2.2 Mathematical Model

The governing equations and numerical methods summarized in this section have been implemented in the MPSalsa computer code, developed at Sandia National Laboratories. More complete descriptions of the code and capabilities can be found in the following references.[4,6,20–22]

The fundamental conservation equations for momentum, heat, and mass transfer are presented for a reacting flow application. The equations for fluid flow consist of the incompressible Navier-Stokes equations for a variable-density fluid and the continuity equation, which express conservation of momentum and total mass. The steady-state momentum equation takes the form:

$$\rho(\mathbf{u} \bullet \nabla)\mathbf{u} - \nabla \bullet \mathbf{T} - \rho\mathbf{g} = 0, \tag{1}$$

where $\mathbf{u}$ is the velocity vector, ρ is the mixture density, and $\mathbf{g}$ is the gravity vector. $\mathbf{T}$ is the stress tensor for a Newtonian fluid:

$$\mathbf{T} = -P\mathbf{I} - \frac{2}{3}\mu(\nabla \bullet \mathbf{u})\mathbf{I} + \mu[\nabla\mathbf{u} + \nabla\mathbf{u}^T] \tag{2}$$

Here P is the isotropic hydrodynamic pressure, μ is the mixture viscosity, and $\mathbf{I}$ is the unity tensor. The total mass balance is given by:

$$\nabla \bullet (\rho\mathbf{u}) = 0 \tag{3}$$

The steady-state energy conservation equation is given as:

$$\rho\hat{C}_p(\mathbf{u} \bullet \nabla)T = \nabla \bullet (\lambda\nabla T) - S, \tag{4}$$

where $\hat{C}_p$ is the mixture heat capacity and λ is the mixture thermal conductivity. The last term on the right hand side S is the source term due to the heat of reaction, which is negligible under the process conditions in this system.

The species mass balance equation is solved for N_g-1 gas-phase species:

$$\rho(\mathbf{u} \bullet \nabla)Y_k = \nabla \bullet \mathbf{j}_k + W_k\dot{\omega}_k \qquad \text{for } k = 1, \ldots, N_g\text{-}1, \tag{5}$$

where Y_k is the mass fraction of the k^{th} species, $\mathbf{j}_k$ is the flux of species k relative to the mass averaged velocity $\mathbf{u}$ and $\dot{\omega}_k$ is the molar rate of production of species k from gas-phase reactions. The flux, $\mathbf{j}_k$, is based on a mixture averaged diffusion coefficient formulation:

$$\mathbf{j}_k = -\rho Y_k \frac{D_{km}}{X_k}\nabla X_k - D_k^T \frac{\nabla T}{T} \tag{6}$$

Where X_k is the mole fraction of species k, D_{kj} is the mixture averaged diffusion coefficient, and D_k^T is the thermal diffusion coefficient. The second term of equation (6) represents the effects of thermal diffusion, or the Soret effect, which was found to have a significant effect for this system. Finally, an algebraic constraint which enforces the sum of the mass fractions to equal one, replaces one of the PDE species conservation equations:

$$\sum_{k=1}^{N_g} Y_k = 1 \qquad \text{for } k = N_g \tag{7}$$

The physical and transport properties in the above equations are dependent on the thermodynamic pressure and the local temperature and composition. These properties are computed using the Chemkin library.[23] These terms add considerable nonlinearity to the problem and complexity in forming the residual equations. For example, the density is computed from the ideal gas law,

$$\rho = \frac{P_o}{RT}\sum_{j=1}^{N_g} W_j X_j, \tag{8}$$

where P_o is the thermodynamic pressure, R is the gas constant, T is the temperature, X_j is the mole fraction of the j^{th} species, W_j is the molecular weight of the j^{th} species, and N_g is the number of gas-phase species (which is 2 for the model in this paper).

2.3 Boundary Conditions and Operating Parameters

In this section, the boundary conditions for our model will be described, several of which are operating parameters and also variables

in the parameter and optimization studies. Four of the parameters were chosen because they can be set fairly easily by a reactor operator to alter performance. These are the reactor pressure P, the inlet flow velocity V_i, the susceptor rotation rate Ω, and the purge flow rate V_p. The temperature of the reactor top T_t is not easily computed, but is varied primarily as a sensitivity study. However, its value can be altered by reactor design and operation. The final parameter α, defined below, is a first order attempt to capture the effects of feeding the reactant in other than a spatially uniform profile.

The only parameter varied in our study that is not a boundary condition is the reactor pressure, which has a base value of $P = 0.85$atm (approximately the atmospheric pressure in Albuquerque, New Mexico).

In our model, the boundary conditions at the inlet to the reactor (which is $15cm$ wide by $3cm$ high) specify a plug flow velocity, a constant temperature, and the mole fractions of TCS and H_2. The inlet velocity is one of the parameters in the model and has a base value of $V_i = 30$cm/sec. The inlet gas temperature is fixed at $300K$. The mole fraction of TCS at the inlet has an average value of 2.4%. In one parameter study, the mole fraction of TCS is allowed to vary linearly across the reactor width while always maintaining an average of 2.4%. This is a first order model of the effects of spatially varying the inlet concentration profiles. The parameter α controls this variation *via* the following boundary condition for TCS mole fraction at the inlet:

$$X_{TCS} = 2.4\% \left(1.0 + \alpha \frac{y}{W/2}\right). \tag{9}$$

Here y is the crosswise dimension and the inlet covers $-W/2 < y < W/2$, so to keep the mole fraction non-negative the parameter has a range of $-1.0 < \alpha < 1.0$. The base value is $\alpha = 0.0$ which creates a uniform inlet concentration.

The wafer and susceptor surfaces are treated identically in the model except the post-processing of the deposition rate is only performed on the wafer. These surfaces rotate (counterclockwise as viewed from above), are held at a constant temperature of $1323K$, and have the surface deposition model turned on. In general the deposition model can be very detailed,[15] but we have used a simple transport-limited mechanism, where TCS deposits silicon on the surface with a sticking coefficient of unity. The surface Chemkin library[24] is used to calculate the flux of TCS and the deposition rate for post-processing. With no gas phase reactions and this simple surface model, we just have two species equations in the reactor, one for TCS and the other for the hydrogen carrier gas.

The disk rotation is performed through velocity boundary conditions and does not require any movement of the mesh, which is valid

with the assumption that any surface reactions equilibrate instantaneously compared to the rotation period. With a second assumption that the growth run is long compared to the rotation period, the radial deposition profile can be computed by averaging the azimuthal component. The rotation rate Ω is one of the parameters in the model with a base condition of $\Omega = 100$ RPM.

As mentioned in the previous section, our model allows for a purge flow of pure H_2 to enter through the small gap section between the susceptor and the fixed reactor. This velocity of this flow is a parameter with base value of $V_p = 0.0$ and Dankwerts boundary conditions are used to specify the convective flux of the species while not constraining the diffusive flux. Natural boundary conditions of no shear stress are imposed on this surface for the momentum equation components that are tangential to this surface.

The top of the main cylindrical chamber of the reactor ($r < 15cm; z = 3cm$) is held in our model at a uniform temperature. The value is a parameter with a base value of $T_t = 600K$. The actual temperature at the top of the reactor varies spatially and is a very complicated balance between convection, conduction, and radiation, but whose calculation is beyond the scope of this effort. While this parameter can not be set in a typical reactor as readily as most of the other parameters, the temperature of the reactor top can be influenced by reactor design.

The outlet of the reactor uses a pressure boundary condition on the normal momentum equation that (weakly) sets the normal gradient of the normal velocity to zero. All boundary conditions not specified above are no-slip on tangential velocities, no-penetration on the normal velocity, an adiabatic (no-flux) condition on the heat equation, and no-flux condition on the species balances.

3 Solution Methods

The above system of 7 coupled PDEs (Equations 1, 3, 4, 5) and boundary conditions are solved for unknowns $\mathbf{u}_x$, $\mathbf{u}_y$, $\mathbf{u}_z$, P, T, Y_{TCS}, and Y_{H_2} with the MPSalsa code. MPSalsa uses a Galerkin/least-squares finite element method[22,25,26] to discretize these equations over the spatial domain. This stabilization procedure allows for the use of equal order linear FE basis functions for all variables while avoiding spurious pressure oscillations for incompressible flows. The stabilization also incorporates a streamline upwind Petrov-Galerkin (SUPG) type methodology for controlling oscillations due to convective effects. An additional important aspect of this stabilization procedure is that a fully-implicit (for time dependent systems) and a direct-to-steady-state solution procedure using Newton-Krylov methods can be implemented.[22] These robust non-linear and linear solvers are essential for

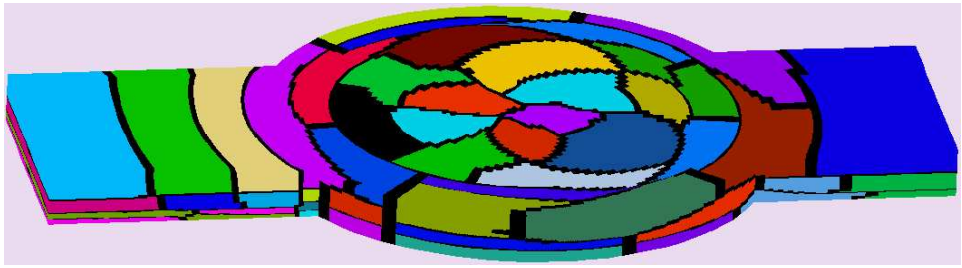

Figure 2: A visualization of the partition of the 182853 node mesh for 100 processors is shown. The colored patches are elements (in the finite element discretization) whose nodes are all owned by a given processor, while the black strips are elements whose nodes are owned by multiple processors. Interprocessor communication is needed only across these elements for performing the finite element method.

efficiently converging the continuation and optimization methods we briefly describe in the following sections.

Th MPSalsa code is designed for general unstructured meshes in 2D and 3D, and runs on massively parallel computers. The results in this paper were calculated for a mesh of 174080 (eight-node trilinear hexahedral) elements and 182853 nodes, which corresponds to nearly 1.3 Million equations and unknowns. The mesh is produced using the CUBIT software[27] and decomposed for parallel solution using the Chaco graph partitioning package.[28,29] The partitioner assigns each node to a processors in a way to evenly distribute the work load while minimizing interprocessor communication. The decomposition of the mesh for 100 processors is visualized in Figure 2. Finite elements with all eight corner nodes owned by the same processor are given a color unique to that processor. Elements broken over multiple processors are colored black, and indicate the amount of information that need to be communicated to perform a matrix fill or matrix-vector multiply.

3.1 Non-linear/Linear Solution Methods

A fully coupled inexact Newton's method is used to robustly calculate steady-state solutions. For the majority of the results in this paper, the numerical Jacobian option was used. This option calculates the dense Jacobian contribution for each finite element using first order finite differencing. A much more efficient analytic Jacobian fill routine exists yet does not include all the dependencies for this case where the physical and transport properties depend on the local composition.

The Newton iteration to find the solution to the discretized equations, $\mathbf{f}(\mathbf{x}) = 0$, is simply,

$$\begin{aligned} \mathbf{J}\delta &= -\mathbf{f}(\mathbf{x}), \\ \mathbf{x}^{new} &= \mathbf{x} + \theta\delta. \end{aligned} \tag{10}$$

Here $\mathbf{J}$ is the Jacobian matrix ($d\mathbf{f}/d\mathbf{x}$), δ is the solution update vector, and θ is a damping coefficient. This coefficient is bound by $10^{-4} \leq \theta \leq 1.0$ and set less then 1.0 only when a full Newton step $\mathbf{x} + \delta$ would result in a negative mole fraction. This damping of the Newton step has been found to make Newton's method more robust for these problems. The iteration is terminated when each component of the Newton update, δ, is small relative to the corresponding component of the current solution, $\mathbf{x}$. This large sparse linear system in Eq.10 is solved approximately at each iteration using the Aztec package of parallel, preconditioned iterative solvers. We selected the ILU preconditioner (with 0 or 1 level of overlap) and the GMRES solver with no restarts.

The majority of the results in this paper were generated on 100 processors of the Sandia-Intel TFlop machine, each of which is a 333MHz Pentium Pro processor. For this problem, a typical matrix formulation required 44 seconds for the inexact analytic Jacobian and 320 seconds to calculate the (nearly) exact finite difference numerical Jacobian. A typical linear solve required 150 GMRES iterations and 220 seconds. Typically $4-6$ Newton iterations where required to converge the nonlinear problem, though occasionally as many as 12 iterations were needed for large jumps in parameter when the Newton update was damped to insure the mass fractions stayed positive after every iteration.

3.2 Continuation Methods

Parameter continuation methods have been implemented in MPSalsa via the LOCA library.[10,30] These methods find families of solutions $\mathbf{x}(\lambda)$ which are parameterized by a system parameter λ. Continuation algorithms have identified multiplicity in vertical CVD reactors.[13,31,32] For this work, there was no solution multiplicity detected so natural continuation with a first-order (Euler-Newton) predictor was sufficient to follow solution branches. The predictor step requires on additional linear solve to calculate the local tangent to the solution curve, $\mathbf{z}$. This tangent is then used, along with a user select parameter step size ($\Delta\lambda$) to create a new solution vector as an initial guess for the next Newton

iteration,

$$\begin{aligned} \mathbf{J}\mathbf{z} &= -\frac{d\mathbf{f}}{d\lambda}, \\ \mathbf{x}^{new} &= \mathbf{x} + \Delta\lambda\mathbf{z}, \\ \lambda^{new} &= \lambda + \Delta\lambda. \end{aligned} \tag{11}$$

A complementary capability to the continuation algorithm is a linear stability analysis, which verifies that the computed steady-state solutions are stable to small perturbations. We have implemented this capability in LOCA using the ARPACK library[10,33] to approximate the few rightmost eigenvalues of the linearized time dependent problem. This method has previously been described in detail[34] and applied to large buoyancy-driven flow problems.[35]

3.3 Optimization Methods

Optimization studies were performed using the Dakota framework,[11] which provides a flexible interface between application codes and numerous algorithms, such as optimization, uncertainty analysis, parameter estimation and sensitivity analysis. It also automates generating gradients of the objective function with respect to parameters by finite differences, when analytic gradients are not available, and implements multi-level parallelism, where significant improvements in computational efficiencies can be realized. In this study we exclusively used a BFGS sequential quadratic programming algorithm (SQP). This is a gradient-based algorithm and requires the complete nonlinear solution of the underlying PDE problem every time the parameters are changed. (to investigate large design and state spaces, alternatives to this approach are being developed.[14,36]) Based on previous experience, the nonlinear solver tolerance was dropped 1 order of magnitude over continuation runs to reduce noise in objective function, particularly in numerical gradient calculations.

The post-processing of the deposition rate profile warrants a quick discussion. The deposition rate on the wafer gives an instantaneous snapshot on the 2D surface, $d(r, \theta)$ (where r and θ are the traditional polar coordinates). The effect of rotation is to average out the θ (azimuthal) component of the deposition rate to render only a radially-varying profile, $d(r)$. This was performed as a post-processing step, by averaging the deposition rate at each of 190 equally-spaced angles for each of 50 different radii. The resulting radial profiles are shown in many of the figures in the results section. The quality of a given growth run is measured by the uniformity of the radial profile. We use two metrics for uniformity in this paper. The first is the non-uniformity, defined as

$$\text{Non-Uniformity} = \left(\max\left[d(r)\right] - \min\left[d(r)\right]\right) / \left(\text{average}\left[d(r)\right]\right). \tag{12}$$

and usually reported in percent. This is an L^∞ norm of the variability of the profile about. The second metric is the L^2 norm of the profile about its average and is used as an objective function in the optimization calculations (see Eq. 13).

4 Parameter Continuation Results

In this section we first present the solution at base operating conditions and then the results of 6 parameter studies about that state point. Optimization results are deferred to the following section. Continuation and optimization are complementary capabilities. Continuation runs give information on the effects of individual parameters and the relative sensitivity of the model to each parameter which in turn optimization methods can utilize as approprate initial conditions. Suitable optimization algorithms can then efficiently find the right combination of parameters for the best design.

4.1 Solution at Base Conditions

The reactor model presented in section 2 was first solved at the base conditions for the 6 operating parameters, as presented in Table 1. The steady solution was reached by a series of steady-state continuation steps and mesh sequencing as follows: 1) on a relatively coarse mesh, the fluid flow was solved for at low pressure and at constant temperature and mass fractions from a trivial initial guess, 2) the pressure was increased to realistic conditions over a series of steps, 3) the temperature was raised to realistic conditions over a period of several steps, 4) the surface reaction was turned on and finally 5) the mesh was refined by hand in regions of steep gradients, and the solution interpolated to the finer mesh. This guess was then reconverged on the finer mesh, which corresponds to 1.3 million unknowns.

A visualization of the three-dimensional solution is given in Figure 3, and shows the large effect of the disk rotation on the streamlines and on the contours of TCS along the bottom surface (which directly correspond to the silicon film growth rate). One feature to note is the peak (in green) of higher deposition toward the far side of the reactor, which falls underneath the spiraling streamlines.

A more quantitative result, seen in Figure 4, is the contour plot of the instantaneous deposition rate along the wafer surface. The expected result of reactant depletion can be seen, with higher deposition rates at the leading (left) edge of the wafer and lower rates on the trailing (right) side. An interesting (and to us, unexpected) feature was the peak in deposition rate on the upper part of this figure. This is the part of the disk carrying fluid against main direction of flow

Parameter	Description [Units]	Min	Max	Base
V_i	Inlet Velocity [cm/sec]	20	50	30
Ω	Rotation Rate [RPM]	0	250	100
P	Reactor Pressure [atm]	0.1	1.2	0.85
V_p	Purge Flow Velocity [cm/sec]	0	100	0
T_t	Temperature of Reactor Top [K]	400	800	600
α	Slope of TCS Feed Conc. [ ]	-1.0	1.0	0.0

Table 1: This table presents the 6 key parameters in this study, along with their minimum, maximum, and base values. The parameters are described in Section 2.1.

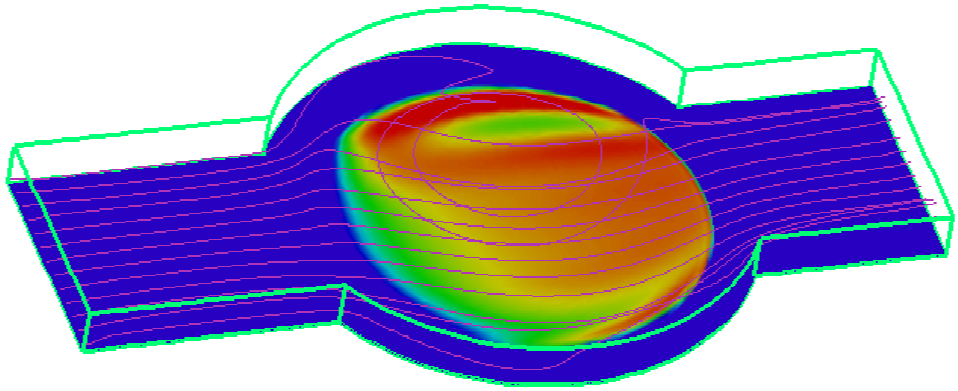

Figure 3: Streamlines through the CVD reactor are shown at the base conditions. The contours of TCS mass fractions, which directly correspond to the deposition rate, are shown along the bottom surface of the reactor. The light blue and green are relatively high concentrations, and red contours are the lowest.

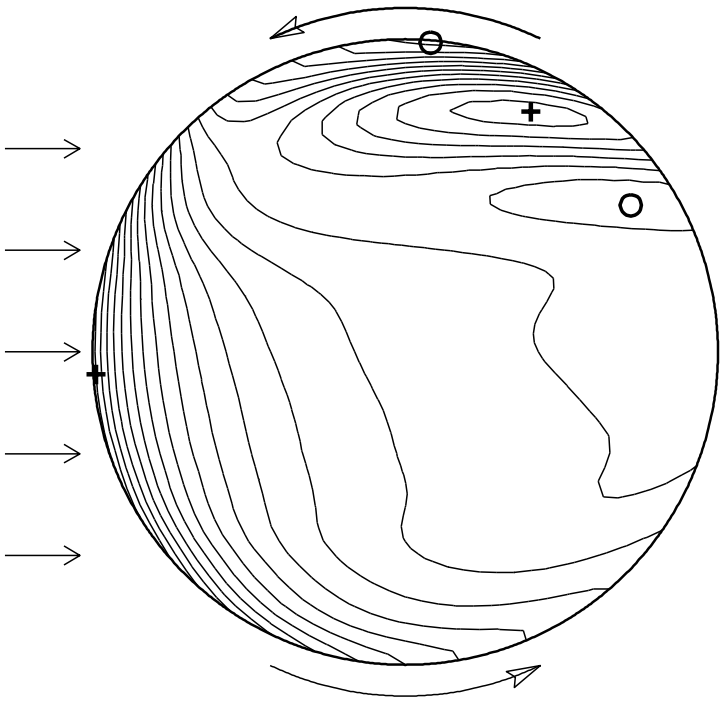

Figure 4: A contour plot of instantaneous deposition rates on the wafer is shown, along with straight arrows showing the predominant flow direction and curved arrows showing the rotation direction. The + symbols mark the positions of local maximum in the deposition rate and the **o** symbols mark minima.

through the reactor, and one might have expected a very low growth rate with the fluid at this point already having rotated three-quarters of the way around the reactor and greatly depleting the TCS. Rather, the source of this peak can be seen in Figure 3, where a recirculation in the flow is above this part of the disk. The spinning disk below the recirculation appears to act as a pump, pulling down fresh reactant to the wafer surface.

The instantaneous deposition over the wafer is averaged with respect to the angle to capture the effects of disk rotation, generating a radial deposition rate profile. This averaging is justified because the period of wafer rotation is much shorter then a typical growth run. This is shown in Figure 5 for a solution at the base conditions, and exhibits a marked increase in deposition rate at larger radii. The non-uniformity of growth over the wafer (defined in Eq. 12) is calculated

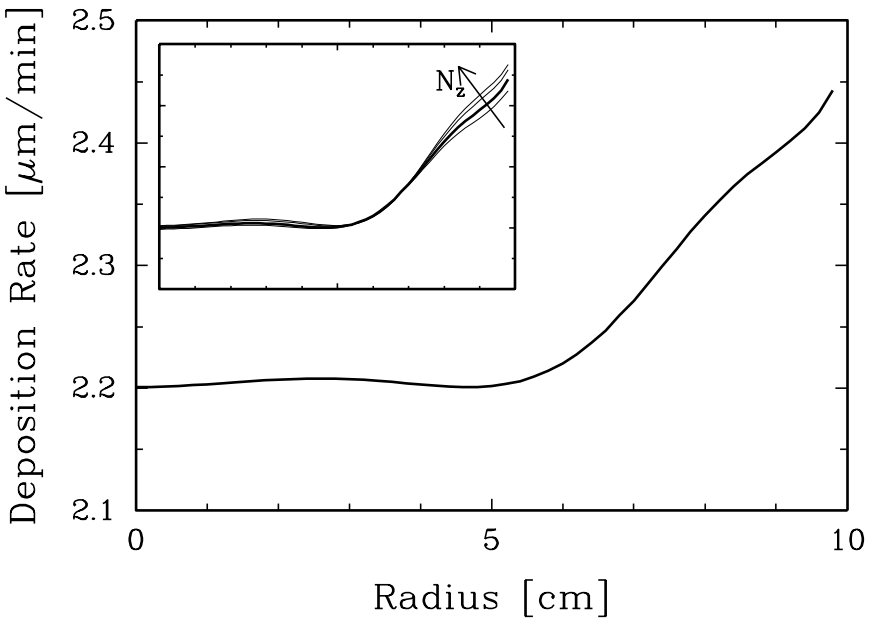

Figure 5: The averaged deposition rate profile at base conditions, calculated by averaging out the azimuthal (θ) component from Figure 4, is shown. Inset: Mesh resolution study with number of elements in Z direction N_z of 24, 32 (bold), 48, and 64.

to be 10.7%, which is well above the desired value of 1%. The inset in this figure is a mesh resolution study for the number of elements in the vertical Z direction. In addition to the mesh with 32 elements in the Z direction, highly graded towards the bottom, the deposition profile was calculated for meshes with 24, 48, and 64 elements. Doubling the mesh in this direction made less then 1% difference in the deposition rate.

In the following six subsections, the effect of the six parameters shown in Table 1 on the radial deposition rate profiles and the non-uniformity are investigated through continuation runs. In each case, the other 5 parameters are held fixed at the base conditions. The continuation was automated using the LOCA software.[10]

4.2 Inlet Velocity, V_i

Parameter continuation on the inlet velocity V_i was performed, and deposition profiles calculated for velocities (in cm/sec) from 20 to 50 in steps of 5. The deposition profiles in Figure 6(A) show that the

overall deposition rate increases weakly with increasing flow rate. This trend is expected since the increase in velocity decreases the boundary layer thickness through which the reactant must diffuse to reach the hot wafer surface. The deposition appears to become more uniform at lower inlet velocities, an observation that is quantified in Figure 7(A). The non-uniformity at higher velocities is due to a growing peak in the deposition rate at large radii. Visualization of the instantaneous (2D) deposition contours show an intensification of the peak in the deposition profile on the part of the disk that is pushing fluid against the main flow direction. The is attributed to the strengthening of the recirculating flow that can be seen in Figure 3 and discussed in the previous section.

4.3 Rotation Rate, Ω

Parameter continuation on the substrate rotation rate Ω was performed, and deposition profiles calculated for rotation rates (in RPM) from 0 to 250 in steps of 25. (The $\Omega = 0$ solution, which is still averaged over wafer rotation, represents the limit of small rotation rates which have negligible impact on the convection yet with a period still much less then a typical growth run.) The deposition profiles in Figure 6(B) show that a peak in the deposition profile near radius of 7 develops at higher rotation rates. This peak intensifies with increasing rotation rate, is the same one discussed in section 4.1 and seen in the instantaneous 2D deposition plot in Figure 4. Overall, the deposition rates increases with rotation rate. The non-uniformity of the deposition rate is observed in Figure 7(B) to be a strong function of the rotation rate, and reaches a minimum of about 4% at $\Omega = 175$.

4.4 Pressure, P

Parameter continuation on the reactor pressure P was performed, and deposition profiles calculated for operating pressures (in atm) from 0.1 to 1.2 in steps of 0.1. The profiles are shown in Figure 6(C). Overall, the deposition rate increases as a strong function of the pressure due to a direct increase density *via* the ideal gas law. An increase in density increases the concentration of the reactant and decreases the boundary layer thickness through which the reactant must diffuse to reach the reacting surface. The profiles show deposition at the edge of the wafer increasing disproportionately to that near the center at high pressures. This is the same effect as seen when increasing the inlet velocity. This is expected since the development of the recirculation is a function of the Reynolds number, which is proportional to both the velocity and density. The non-uniformity of the deposition rate is seen in Figure 7(C) to be a nonlinear function of the pressure, reaching a minimum

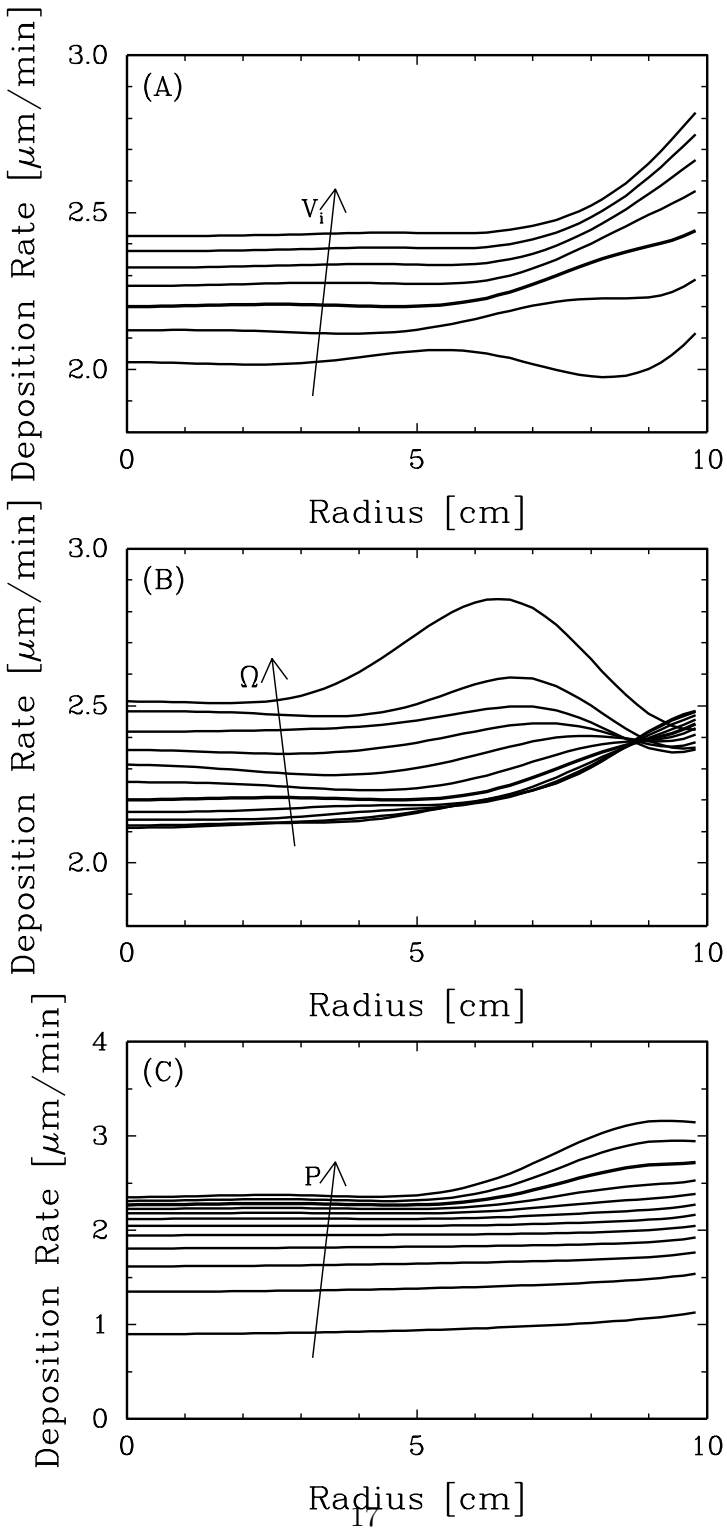

Figure 6: Radial deposition rate profiles of silicon over the wafer calculated for the first three parameters are shown: (A) inlet velocities $V_i = 20 \rightarrow 50$ in steps of 5 (with $V_i = 30$ in bold), (B) rotation rates (in RPM) of $\Omega = 0 \rightarrow 250$ in steps of 25 (with $\Omega = 100$ in bold), and (C) reactor pressures $P = 0.1 \rightarrow 1.2$ in steps of 0.1 (with $P = 1.0$ in bold).

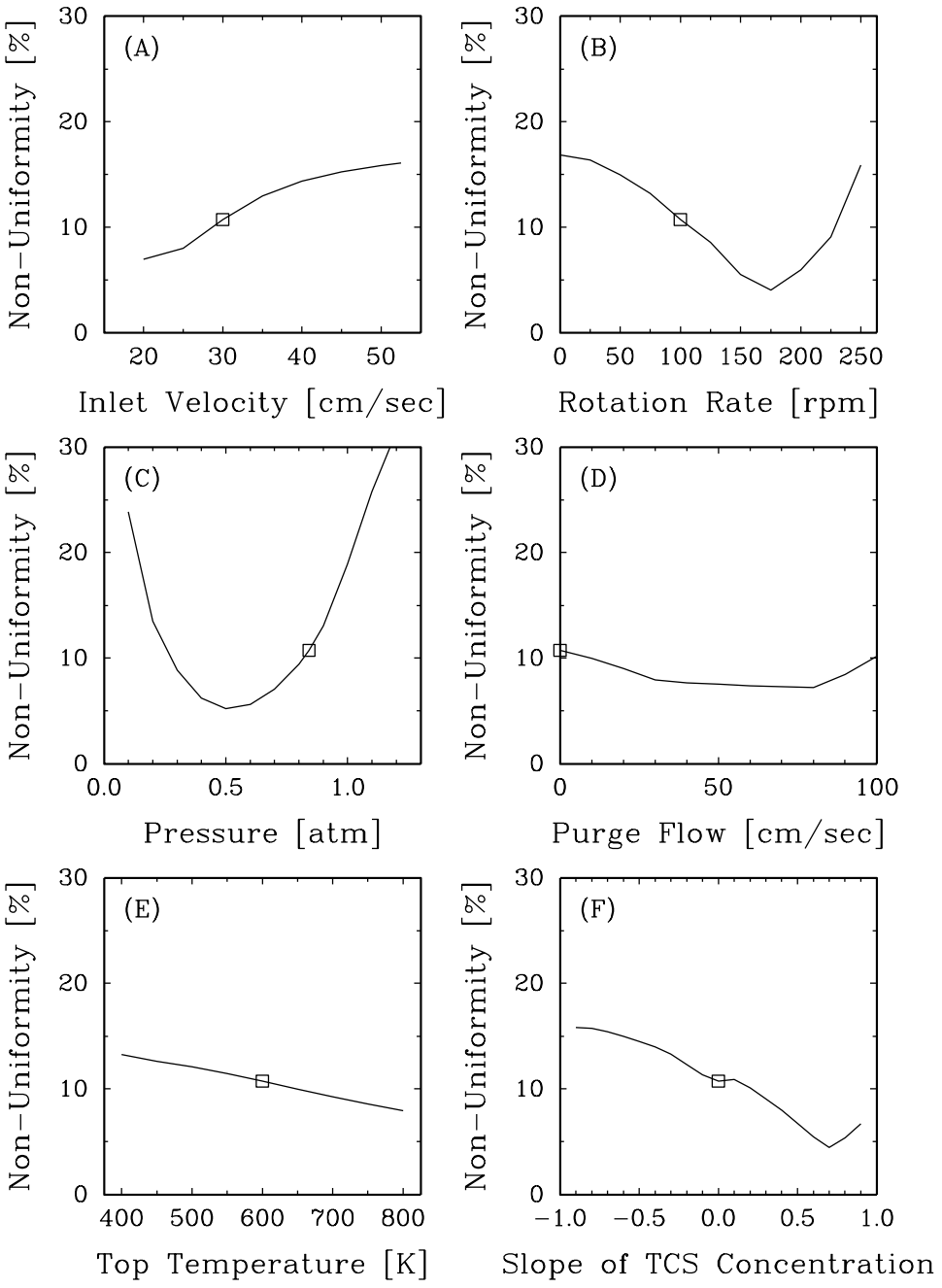

Figure 7: Non-uniformity of deposition rate is plotted as a function of each of the 6 key parameters: (A)inlet velocity V_i, (B) rotation rate Ω, (C) operating pressure P, (D) velocity of the purge flow V_p, (E) temperature of the top of the reactor T_t, and (F) slope of the TCS feed concentration α, where the square symbol represents base conditions.

of about 5% at $P = 0.5$ while reaching over 30% at $P = 1.2$.

4.5 Purge Flow Velocity, V_p

Parameter continuation on the purge flow velocity V_p was performed, and deposition profiles calculated for velocities from 0 to 100 in steps of 10. (The purge flow is the pure H_2 gas pumped into the reactor in the small gap between the rotating substrate and the fixed reactor, and prevents diffusion of reactants and subsequent deposition on reactor parts under the substrate.) The deposition profiles in Figure 8(D) show that a strong purge flow decreases the overall deposition rate, presumably by diluting the reactants. There is also strong decrease at the edge of the wafer, which is likely due to the creation of a boundary layer of pure H_2 through which reactants must diffuse. The non-uniformity of the deposition rate is seen in Figure 7(D) to be a strong function of the purge velocity and reaches a minimum of about 7% at $P = 80$. The discontinuity in slope of this curve at $V_p = 80$ is an expected feature of an L^∞ norm (see Eq. 12), since position of the minimum deposition rate jumps from a radius of near 5 to 10.

4.6 Temperature of Reactor Top, T_t

Parameter continuation on the temperature of the reactor top T_t was performed, and deposition profiles calculated for temperatures from 400 to 800 in steps of 50. The temperature at the top of the reactor is not typically independently controlled nor a constant, yet the result of a balance between radiation, conduction, and convection, and so a function of many design and operating parameters. This study is in part a sensitivity analysis with respect to an unknown quantity, yet the results can also guide reactor design and operation which can alter this temperature in practice. The deposition profiles in Figure 8(E) show that an increase in the reactor top temperature increases the overall deposition rate. We believe this is primarily due to a decrease in thermal diffusion (the Soret effect) when there is a decrease in the temperature gradient normal to the reacting surface. This assertion is supported by the deposition profile for $T_t = 600$ with thermal diffusion turned off in the model, shown with symbols in the same figure. A higher temperature at the top of the reactor also increases deposition due to an increase in overall flow velocity, thereby decreasing the boundary layer thickness, and an increase in molecular diffusion to the surface. The non-uniformity of the deposition rate is seen in Figure 7(E) to be a relatively strong, monotonically decreasing, function of the temperature.

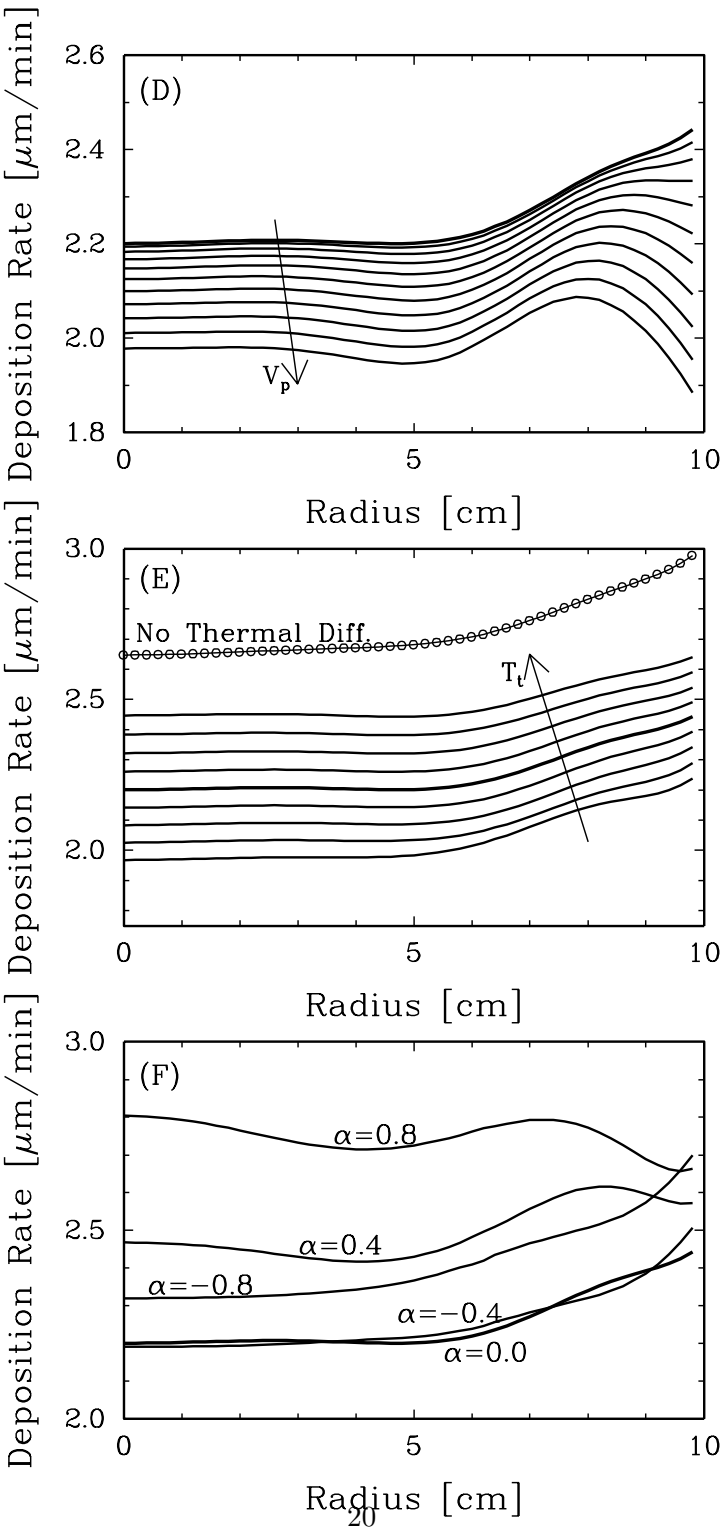

Figure 8: Radial deposition rate profiles of silicon over the wafer calculated for the second set of three parameters are shown: (D) purge flow velocities (in cm/sec) of $V_p = 0 \rightarrow 100$ in steps of 10 (with $V_p = 0$ in bold), (E) reactor top temperatures (in cm/sec) of $T_t = 400 \rightarrow 800$ in steps of 50 (with $T_t = 600$ in bold, and a profile for $T_t = 600$ with the thermal diffusion term turned off in hte model is marked with symbols), and (F) slope of the TCS feed concentration for $\alpha = -0.8 \rightarrow 0.8$ in steps of 0.4 (with $\alpha = 0$ in bold).

4.7 Slope of TCS Feed Profile, α

Parameter continuation was performed on the slope of the feed concentration of the reactant TCS, α, defined in Eq. 9. Deposition profiles were calculated for slopes from -0.9 to 0.9. The dependence is not symmetrical in α becaus the substrate rotation breaks the symmetry of the reactor model about the $y = 0$ mid-plane. As described in Section 2, this parameter is a first order attempt to represent the flexibility in the spatial distribution of reactant feed concentrations. The deposition profiles in Figure 8(F) show that a shape of the deposition profile is a strong function of this parameter. The non-uniformity of the deposition rate is seen in Figure 7(F) to have a minimum near 4% at $\alpha = 0.7$, and another local minimum near $\alpha = -0.1$. It is critical to know that the non-uniformity can have multiple minima for performing the optimization calculation.

5 Optimization Results

The parameter studies presented in the previous section show that the non-uniformity of silicon deposition over the wafer is highly dependent on all 6 of these parameters. Four of the continuation runs showed minimum values on the interior of the parameter range. However the lowest value of the non-uniformity achieved by varying 1 parameter at a time was 4% (for $\Omega = 175$) which is well above the 1% design goal.

To take advantage of the computational efficiency of gradient-based optimization algorithms, the L^2 norm of the radial deposition profile about its average was used. The non-uniformity used in the previous plots, while being a more intuitive metric, is a L^∞ norm which can have discontinuous derivatives and therefore not suitable for gradient based methods. The objective function was calculated numerically from the deposition radial profiles as follow:

$$ObjFn = \left(\frac{1}{A} \int (\frac{d(r)}{\bar{d}} - 1)^2 r dr \right)^{1/2} \tag{13}$$

where A is the wafer area, $d(r)$ is the radial deposition profile, and $\bar{d}$ is the average of the profile, pre-calculated by integrating $d(r)$. The results of the six parameter runs are re-plotted with this objective function in Figure 9. The parameter ranges of the X-axis are kept the same as in the previous plots. It can be seen that this objective function closely tracks the non-uniformity metric used above yet is more smoothly varying, with a minimum value of $ObjFn = 0.013$ corresponding approximately to 4% non-uniformity.

Four optimization calculations were performed for this reactor using the BFGS SQP algorithm and finite-differenced gradients. The results

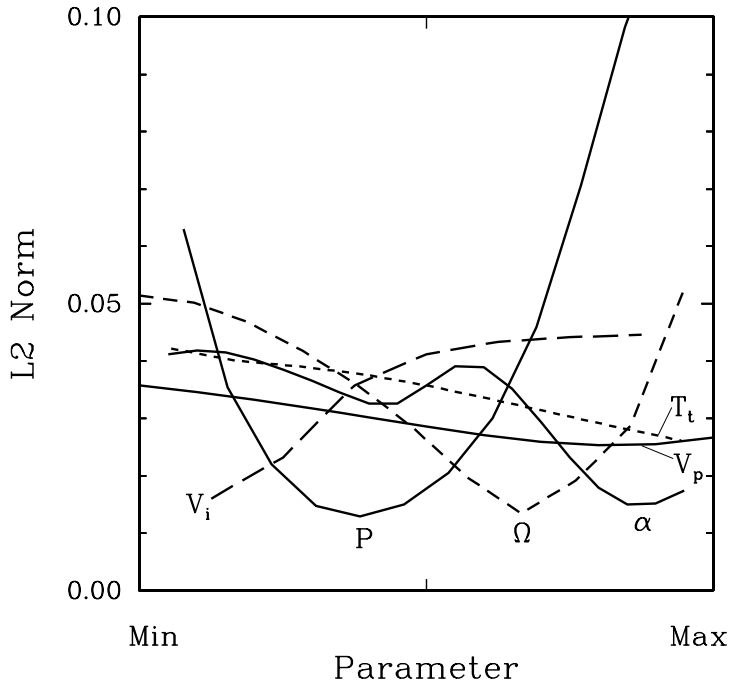

Figure 9: The results of the 6 parameter studies in the previous section are re-plotted using the L^2 norm of the variation in the radial deposition profile (see Eq. 13) as a measure of non-uniformity instead of the L^∞ norm (in Eq. 12). This metric, though less intuitive, has continuous derivatives which makes it more amenable to gradient-based optimization algorithms.

Parameter(s) Varied	Final Value(s)	Non-Uniformity	$ObjFn$
Ω	(176.1)	3.98%	0.0136
P	(0.491)	5.23%	0.0129
V_i, Ω, P	(37.0, 207.6, 0.608)	0.99%	0.00195
V_i, Ω, P, V_p, T_t, α	(21.4, 170.3, 0.327, 79.3, 800., -0.070)	0.10%	0.000192

Table 2: This table summarizes the results of 4 different optimization runs.

are summarized in Table 2, and show the minimum objective function (L^2 norm) as well as the corresponding non-uniformity (L^∞ norm). In all cases, the parameters not being optimized were held at the base conditions in Table 1.

The first two were verification runs, each varying only one parameter, so that the results could be compared with the continuation runs. The first one changed the rotation rate parameter Ω and the second changed the Pressure P. Each produced results consistent with the results of the continuation runs, as read from the curves in Figures 7(B) and 7(C).

The third run varied the first 3 parameters in Table 1, the Inlet Velocity V_i, the Rotation Rate Ω, and the Pressure P. Of all the parameters considered in this study, these three are most conducive to adjustments by a reactor operator. This run converged in 20 iterations of the BFGS SQP algorithm. The MPSalsa code was launched 143 times, 60 of which were for numerical gradient calculations (3 parameters $\times$ 20 iterations) and the remaining 83 for the line searches. The steady-state calculations took an average of 4.6 Newton iterations to converge, with a maximum of 9. The total compute time was approximately 50 hours on 200 processors. Figure 10 shows the migration of the Ω and P parameters throughout the run. About 13 of the line searches can be visually distinguished on this plot.

The final run was on all 6 parameters in this study and achieved the largest reduction in the objective function. The objective function dropped 1 order of magnitude from the 1-parameter runs to the 3-parameter run, and an additional order of magnitude in the 6-parameter run. The non-uniformities dropped from 3.98% for optimization on Ω, to 0.99% for the 3-parameter run, to 0.10% in the 6-parameter study. The radial profiles for the optimal solution found in each of the four runs is shown in Figure 11. The improvement in uniformity with increasing numbers of optimization parameters can be clearly seen. Another interesting feature is that the average deposition rate, which does not appear in the objective function, varies significantly between the runs.

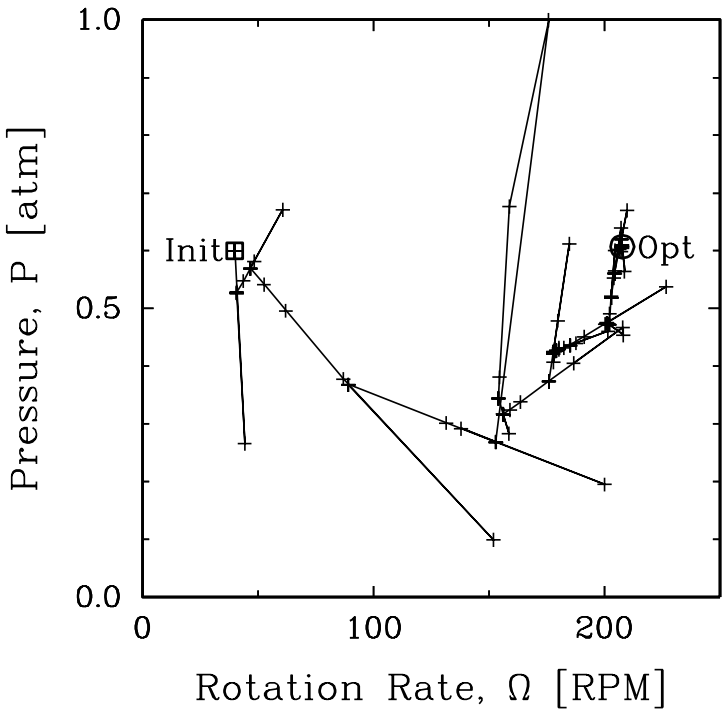

Figure 10: The path of two of the parameters during the 3-parameter optimization run (V_i not shown) is shown. The initial guess and optimal values are labelled. The individual solutions are marked with + and solutions that are part of a line search are connected with a line.

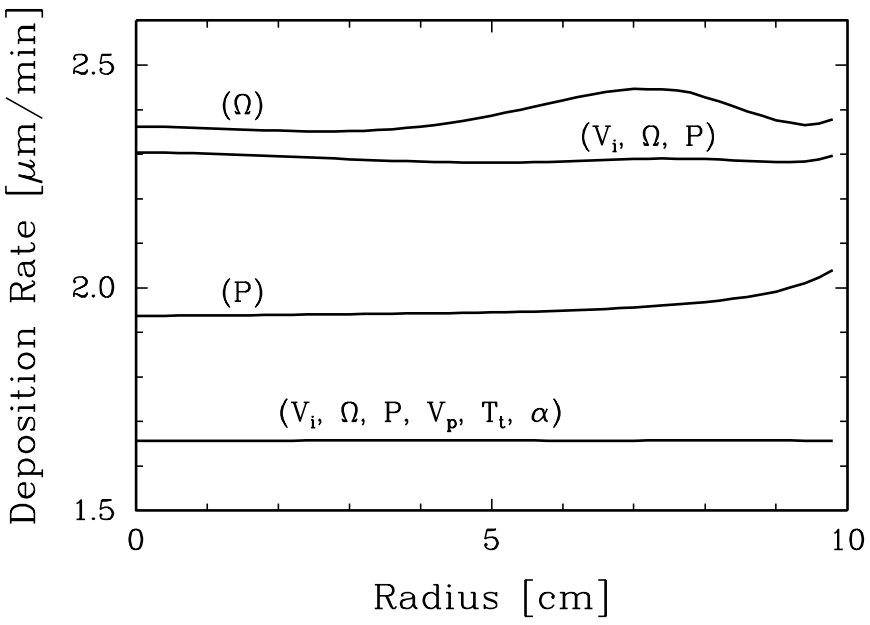

Figure 11: Radial deposition profiles for the optimum solution for each of four different optimization runs are shown. The profiles are labelled with the parameter(s) allowed to vary in the optimization run. The objective function for the runs was the L^2 norm of the variation of these profiles (see Eq. 13).

The instantaneous deposition for the 6-parameter optimum is shown in Figure 12. (After averaging out the effects of rotation, this profile produces the flat profile in Figure 11.) The maximum deposition rate is about 2.5 times that of the minimum, so the profile is not flat; however, a linear variation diagonally across the disk is nearly achieved.

A sensitivity analysis was performed to give information on the sensitivity of the optimal solution with respect to the parameters, as well as to verify the result. Each of the six parameters was perturbed around its optimal value (as shown in the last row of Table 2) by $\pm 1\%$ of its range (as bracketed by the Min and Max columns of Table 1). The ratio of the objective function at the perturbed parameter value to the minimum objective function is shown in Table 3. The optimum is seen to be most sensitive to the operating pressure, where a 1% (0.011 $[atm]$) perturbation in either direction results in a 14-fold increase in the objective function. The only parameter with a weak influence is the temperature at the top of the reactor.

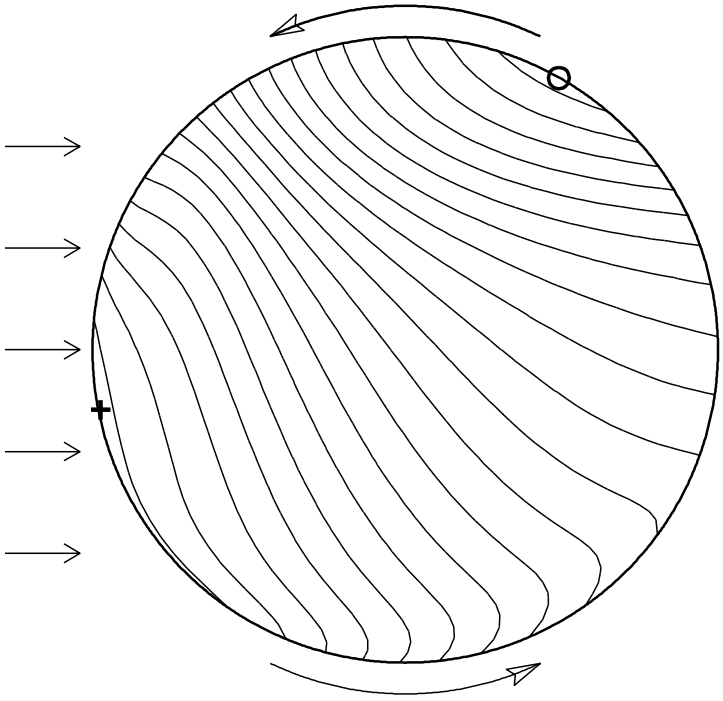

Figure 12: Contours of the instantaneous deposition profile for the optimal solutions found in the 6-parameter run are shown. The + marks the position of the maximum deposition rate and the **o** marks the minimum.

Parameter Varied	-1% perturbation	$+1\%$ perturbation
V_i	1.94	1.99
Ω	2.19	2.03
P	14.04	13.88
V_p	2.04	2.28
T_t	1.13	1.27
α	5.35	5.26

Table 3: Results of a sensitivity analysis around the optimum of the 6-parameter run. The table entries are relative values of the objective function compared to the optimal value, for each parameter being perturbed 1% of its range in each direction.

As a final verification of the optimal solution, we used our linear stability analysis capability to probe the temporal behavior of the steady solution to small perturbations. There is nothing in our solution algorithms that requires a steady-state solution to be stable, and the literature is rich with reactors that exhibit solution multiplicity. At these conditions, the leading eigenvalue was determined to be a conjugate pair at $-4.8 \pm 1.0i[sec^{-1}]$, with the negative real part confirming that the solution is temporally stable.

We have no reason to expect that the optimum for the 3-parameter and 6-parameter runs are global optima, as opposed to just local minima. We know that local minima can exist from the continuation run on α, which shows two distinct minima in Figure 9. In addition, the final values of V_p and T_t in the 6-parameter run are very close to their initial values of 80 and 800, with much of the parameter space not being explored.

Although the present model is not predictive, we believe that the optimization problem presented here is of the same complexity as one for a model with improved chemistry mechanisms and geometric detail. Therefore, the fact that the non-uniformity can be driven so low is an important finding, even if this locally optimal solution is not the global optimum. Since the 0.10% non-uniformity far exceeds a typical design goal of 1% for this process, the local optimum would likely be good enough. If further examination found multiple regions in parameter space with very low non-uniformities, a more intricate objective function could be formulated to further distinguish them. For instance, the objective function could include not only non-uniformity but also secondary economic factors such as reactant utilization, or even the sensitivity of the non-uniformity to expected variations in the parameters.

The more general result, that falls within the scope of this work, is that optimization of 3D models of the CVD process can be robustly performed on a handful of parameters, and that non-uniformities can be driven low enough that secondary effects can be incorporated into the objective function. Choosing the form of the objective function to accurately weigh design trade-offs is the work of a reactor designer. The calculations here show that the development of robust solution and optimization algorithms can lead to the state where an entire optimization run can replace a single solution as the basic computational unit in the design process.

6 Summary and Conclusions

A 3D model for the growth of epitaxial silicon films in a horizontal CVD reactor was presented and solved. The model includes a fully coupled

PDE model for flow, heat transfer, and mass transfer in the reactor and a simple deposition model on the rotating susceptor surface. An unstructured grid finite element method enabled the representation of the inlet and outlet regions, the rotating susceptor and wafer regions, and the small gap between the rotating and fixed parts of the reactor. The model includes the dependency of the physical and transport properties on the local temperature and composition, including the non-negligible effect of thermal diffusion (the Soret effect). The most serious shortcomings of our current model are the exceedingly simplified chemistry mechanism and the lack of a model for heat transfer in and between (*via* conduction and radiation) the solid surfaces that bound the reactor.

The individual effects of 6 operating parameters on the spatial uniformity of deposition were uncovered with parameter continuation runs. The pressure and susceptor rotation rate were found to have particularly large and nonlinear effects. A large flow rate of purge gas through the gap between the rotating and fixed parts of the reactor was found to greatly decrease the deposition rate near the edge of the wafer, in part counteracting the effect of reactant depletion that puts a peak at the wafer edge. Optimization runs on 1, 3, and 6 parameters produced conditions where the predicted deposition profiles had non-uniformities of 4%, 1%, and a very low 0.10%. These results are visualized in Figure 11, the key figure of this paper.

The automated parameter studies and optimization runs were made possible by the rapid and reliable numerical methods for the solution of coupled PDEs on parallel computers. A typical calculation for our 1.3 Million unknown model, starting with a previous solution at nearby parameters as an initial guess, required just 20 minutes on a 200 processor machine (and 90 minutes on a more accessible 24 node LINUX cluster). On the order of 1000 steady state calculations were performed on this model in less then a month. This represents a significant step in a goal of research into solution and analysis algorithms for 3D models, which is to make these computations efficient and informative enough to become an integral part of the design cycle.

Acknowledgments

The authors would like to thank Pauline Ho of Reaction Design Inc. for information and insight into chemical reaction mechanisms and silicon epitaxy. We would also like to thank John Krueger and Walter Huber of SUMCO USA for motivating our study and imparting considerable insight. We would also like to thank our colleagues on the MPSalsa, Trilinos, and Dakota code projects.

References

1. Moffat, H. K.; Jensen, K. F. Complex phenomena in MOCVD reactors. *Journal of Crystal Growth* **1986,** *77,* 108-119.
2. Moffat, H. K.; Jensen, K. F. 3-Dimensional flow effects in silicon cvd in horizontal reactors. *Journal of the Electrochemical Society* **1988,** *135,* 459-471.
3. Kleijn, C.; Hoogendoorn, C. J. A study of 2-D and 3-D transport phenomena in horizontal chemical vapor deposition reactors. *Chemical Engineering Science* **1991,** *46,* 321-334.
4. Pawlowski, R. P.; Theodoropoulos, C.; Salinger, A. G.; Mountziaris, T.; Moffat, H. K.; Shadid, J. N.; Thrush, E. J. Fundamental models of metalorganic vapor phase epitaxy of gallium nitride and their use in reactor design. *Journal of Crystal Growth* **2000,** *221,* 622–628.
5. Mihopoulos, T. G.; Hummel, S. G.; Jensen, K. F. Simulation of flow and growth phenomena in a close-spaced reactor. *Journal of Crystal Growth* **1998,** *195,* 725-732.
6. Salinger, A. G.; Shadid, J. N.; Hutchinson, S. A.; Hennigan, G. L.; Devine, K. D.; Moffat, H. K. Analysis of gallium arsenide deposition in a horizontal chemical vapor deposition reactor using massively parallel computations. *Journal of Crystal Growth* **1999,** *203,* 516-533.
7. Kommu, S.; Wilson, G. M.; Khomami, B. A theoretical/experimental study of silicon epitaxy in horizontal single-wafer chemical vapor deposition reactors. *Journal of The Electrochemical Society* **2000,** *147,* 1538–1550.
8. Segal, A. S.; Galyukov, A. O.; Kondratyev, A. V.; Sid'ko, A. P.; Karpov, S. Y.; Makarov, Y. N.; Siebert, W.; Storck, P. Comparison of silicon epitaxial growth on the 200- and 300-mm wafers from trichlorosilane in Centura reactors. *Microelectronic Engineering* **2000,** *56,* 93-98.
9. Hutchinson, S. A.; Shadid, J. N.; Tuminaro, R. S. "AZTEC User's Guide: Version 1.0", Technical Report, Sandia National Laboratories, Albuquerque, New Mexico 87185, 1995 SAND95-1559.
10. Salinger, A. G.; Bou-Rabee, N.; Pawlowski, R. P.; Wilkes, E. D.; Burroughs, E. A.; Lehoucq, R. B.; Romero, L. A. "LOCA 1.0: Library of Continuation Algorithms - Theroy and Implementation Manual", Technical Report, Sandia National Laboratories, Albuquerque, New Mexico 87185, 2002 SAND2002-0396.
11. Eldred, M.; Giunta, A.; Van Bloemen Waanders, B.; Wojtkiewicz, S.; Hart, W.; Alleva, M. "DAKOTA, a multilevel par-

allel object-oriented framework for design optimization, parameter estimation, uncertainty quantification, and sensitivity analysis: version 3.0 users manual", Technical Report, Sandia National Laboratories, Albuquerque, New Mexico 87185, 2002 SAND2001-3796.

12. Eldred, M. S.; Hart, W. E.; Bohnhoff, W. J.; Romero, V. J.; Hutchinson, S. A.; Salinger, A. G. Utilizing Object- Oriented Design to Build Advanced Optimization Strategies with Generic Implementation. *Proceedings of the 6th AIAA/NASA/ISSMO Symposium on Multidisciplinary Analysis and Optimization, AIAA-96-4164-CP* **1996,** 1568–1582.

13. Salinger, A.; Pawlowski, R. P.; Shadid, J. N.; van Bloemen Waanders, B.; Bartlett, R. A.; Itle, G. C.; Biegler, L. T. Optimization of Large-Scale Reacting Flows using MPSalsa and Sequential Quadratic Programming. In *Large-Scale PDE-Constrained Optimization*, Vol. 30; Biegler, L.; Ghattas, O.; Heinkenschloss, M.; van Bloemen Waanders, B., Eds.; Springer: New York, 2003.

14. Itle, G. C.; Pawlowski, R. P.; Salinger, A. G.; Shadid, J. N.; Biegler, L. T. A Tailored Optimization Strategy for PDE-based Design: Application to a CVD Reactor. *Computers in Chemical Engineering* **2003,** in press.

15. P., H.; Balakrishna, A.; Chacin, J. M.; Thilderkvist, A.; Haas, B.; Comita, P. B. Chemical Kinetics for Modeling Silicon Epitaxy from Chlorosilanes. In *Fundamental Gas-Phase and Surface Chemistry of Vapor-Phase Materials Synthesis*, Vol. 98-23; Mountziaris, T. J.; Allendorf, M. D.; Jensen, K. F.; Ulrich, R. K.; Zachariah, M. R.; Meyyappan, M., Eds.; The Electrochemical Society: Pennington, NJ, 1999.

16. Ho, P.; Coltrin, M.; Breiland, W. Lased-Induced Fluorescence Measurements and Kinetic-Analysi of Si atom formation in a rotating-disk chemical vapor deposition reactor. *Journal of Physical Chemistry* **1994,** *98,* 10138–10147.

17. Habuka, H.; Nagoya, T.; Mayasumi, M.; Katayama, M.; Shimada, M.; Okuyama, K. Model on transport phenomena and epitaxial growth of silicon thin film in SiHCl3-H-2 system under atmospheric pressure. *Journal of Crystal Growth* **1996,** *169,* 61-72.

18. Swihart, M. T.; Carr, R. W. On the mechanism of homogeneous decomposition of the chlorinated silanes. Chain reactions propagated by divalent silicon species. *Journal of Physical Chemistry* **1998,** *102,* 1542–1549.

19. Pawlowski, R. P.; Salinger, A. G.; Habermehl, S. D.; Ho, P. Modeling of a silane LPCVD process used for microelectronics and MEMS fabrication. *Electrochemical Society Series* **2001,** *2001,* 276–283.

20. Shadid, J. N.; Moffat, H. K.; Hutchinson, S. A.; Hennigan, G. L.; Devine, K. D.; Salinger, A. G. "MPSalsa: A Finite Element Computer Program for Reacting Flow Problems - Part I Theoretical Development", Technical Report, Sandia National Laboratories, Albuquerque, New Mexico 87185, 1996 SAND95-2752.

21. Salinger, A. G.; Devine, K. D.; Hennigan, G. L.; Moffat, H. K.; Hutchinson, S. A.; Shadid, J. N. "MPSalsa: A Finite Element Computer Program for Reacting Flow Problems - Part II User's Guide", Technical Report, Sandia National Laboratories, Albuquerque, New Mexico 87185, 1996 SAND96-2331.

22. Shadid, J. N. A Fully-coupled Newton-Krylov Solution Method for Parallel Unstructured Finite Element Fluid Flow, Heat and Mass Transport. *IJCFD* **1999,** *12,* 199–211.

23. Kee, R.; Rupley, F. M.; Meeks, E.; Miller, J. A. "Chemkin-III: A Fortran Chemical Kinetics Package for the Analysis of Gas-Phase Chemical and Plasma Kinetics", Technical Report, Sandia National Laboratories, Albuquerque, New Mexico 87185, 1996 SAND96-8216.

24. Coltrin, M. E.; Kee, R.; Rupley, F. M.; Meeks, E. "Surface Chemkin-III: A Fortran Package for Analyzing Heterogeneous Chemical Kinetics at a Solid-Surface—Gas-Phase Interface", Technical Report, Sandia National Laboratories, Albuquerque, New Mexico 87185, 1996 SAND96-8217.

25. Hughes, T. J. R.; Franca, L. P.; Balestra, M. A New Finite Element Formulation for Computational Fluid Dynamics: V. Circumventing the Babuska-Brezzi Condition: A Stable Petrov-Galerkin Formulation of the Stokes Problem Accommodating Equal-order Interpolations. *Computer Methods in Applied Mechanics and Engineering* **1989,** *59,* 85-99.

26. Hughes, T. J. R.; Franca, L. P.; Hulbert, G. M. A new finite element formulation for computational fluid dynamics: VII. The Galerkin/Least-Squares method for advective-diffusive equations. *Computer Methods in Applied Mechanics and Engineering* **1989,** *73,* 173-189.

27. Shepherd, J. F. "CUBIT mesh generation toolkit", Technical Report, Sandia National Laboratories, Albuquerque, New Mexico 87185, 2000 SAND2000-2647.

28. Hendrickson, B.; Leland, R. An improved spectral graph partitioning algorithm for mapping parallel communications. *SIAM Journal on Scientific Computing* **1995,** *16,* 452-469.

29. Hendrickson, B.; Leland, R. "The Chaco user's guide: Version 2.0", Technical Report SAND94–2692, Sandia National Labs, Albuquerque, NM, 1995.

30. Salinger, A. G.; Lehoucq, R. B.; Romero, L. Stability Analysis of Large-Scale Incompressible Flow Calculations on Massively Parallel Computers. *CFD Journal* **2001,** *9,* 529–533.

31. Fotiadis, D.; Keida, S.; Jensen, K. F. Transport phenomena in verticle reactors for metalorganic vapor-phase epitaxy 1. effects of heat-transfer characteristics, reactor geometry, and operating conditions. *Journal of Crystal Growth* **1990,** *102,* 441-470.

32. Pawlowski, R. P.; Salinger, A. G.; Romero, L. A.; Shadid, J. N. Computational design and Analysis of MPOVPE Reactors. *Journal de physique IV* **2001,** *11,* 197–204.

33. Lehoucq, R. B.; Sorensen, D. C.; Yang, C. *ARPACK USERS GUIDE: Solutions of Large Scale Eigenvalue Problems;* SIAM: Philadelphia, PA, 1998.

34. Lehoucq, R. B.; Salinger, A. G. Large-Scale Eigenvalue Calculations for Stability Analysis of Steady Flows on Massively Parallel Computers. *International Journal for Numerical Methods in Fluids* **2001,** *36,* 309–327.

35. Salinger, A.; Lehoucq, R.; Pawlowski, R.; Shadid, J. Computational Bifurcation and Stability Studies of the 8:1 Cavity Problem. *International Journal of Numerical Methods in Fluids* **2002,** *40,* 1059–1073.

36. Van Bloemen Waanders, B.; Bartlett, R.; Long, K. R.; Boggs, P. T.; G., S. A. "Large scale non-linear programming for PDE constrained optimization", Technical Report, Sandia National Laboratories, Albuquerque, New Mexico 87185, 2002 SAND2002-0396.